scientific reports

OPEN

Widespread shift toward extreme dominated precipitation with pronounced trends in arid and mediterranean regions

Masoud Zaerpour[1]✉, Simon Michael Papalexiou[1,2] & Guoqiang Tang[3]✉

Understanding how precipitation extremes evolve relative to total precipitation has important implications for hydrology, water resources, and climate risk management. While previous studies have assessed trends in total precipitation and extremes separately, the changing balance between them remains underexplored globally. Here, we use the Extreme Precipitation Fraction (EPF)—the ratio of a year's wettest daily precipitation event to its total annual precipitation—as a physically meaningful metric to quantify the dominance of extremes within annual rainfall totals. Using an ensemble of 25 CMIP6 global climate model simulations from the NASA NEX-GDDP dataset, we examine historical EPF patterns, projected trends under the high-emissions scenario. A first-order relative-change decomposition is then used to quantify the separate contributions of annual maximum daily precipitation and total annual precipitation to EPF trends. Results show that, historically, EPF values are highest in hot and cold deserts, where a single event contributes over 13–15% of annual rainfall, and lowest in tropical rainforest and monsoon zones (< 4%). Projected trends show a global shift toward more extreme-dominated regimes, particularly in dryland and Mediterranean climates. EPF increases exceed + 0.2 per decade in Mediterranean zones, where over 70% of grids show positive trends above + 0.1. In contrast, polar and high-latitude snow-dominated climates exhibit declining EPF values. Attribution of EPF trends to its individual contributions shows that changes in total annual precipitation dominate EPF trends in arid and Mediterranean regions (annual-maximum contribution < 45%), whereas changes in extreme precipitation contribute more strongly in humid temperate and monsoonal regions (> 54%). At high latitudes (> 67.5°N), changes in total precipitation account for more than 70% of EPF trends. These findings reveal that precipitation is increasingly delivered through fewer, more intense events in vulnerable regions, with implications for climate-risk assessment and adaptation planning.

Climate change is intensifying the global water cycle, with strong evidence that atmospheric warming increases the potential for heavy precipitation events, although observed responses vary regionally[1–4]. Because warmer air can hold more moisture (approximately 6–7% per °C of warming or more), the atmosphere has an enhanced capacity to produce intense rainfall[5–8]. Consistent with these thermodynamic expectations, many observational records and climate model simulations indicate increases in the frequency and intensity of heavy precipitation in numerous regions[9–12], though decreases or mixed trends are also reported in some areas such as parts of the Mediterranean and southwestern North America[13–16]. This escalation of extreme rainfall translates into rising flood hazards[17,18] and substantial societal and environmental impacts[19–22], underscoring that intensifying precipitation extremes represent a pressing global concern[23,24].

Precipitation changes under climate change can occur through different pathways, including shifts in total annual precipitation as well as changes in the intensity and frequency of extreme events. Observational records indicate increasing annual precipitation across many mid- to high-latitude and tropical regions, including large areas of North America, northern Europe, West Africa, and monsoonal Asia[3,13,14,25–28], whereas several subtropical and arid regions—such as the Mediterranean basin, southern South America, and Central Asia—

[1]Department of Civil Engineering, Schulich School of Engineering, University of Calgary, Calgary, Canada. [2]Institute of Global Water Security, Hamburg University of Technology, Hamburg, Germany. [3]State Key Laboratory of Water Resources Engineering and Management, Wuhan University, Wuhan, China. ✉email: masoud.zaerpour@ucalgary.ca; guoqiang.tang@whu.edu.cn

have experienced long-term drying trends[13–16]. These contrasting patterns reflect the combined influence of thermodynamic moisture increases and region-specific changes in atmospheric circulation and moisture transport[29–32].

Changes in precipitation extremes exhibit similarly strong regional variability. Pronounced increases in heavy rainfall have been documented across the mid-latitudes of North America and much of Eurasia and South America[33], while other regions show more heterogeneous or less consistent responses rather than clear long-term trends[13–16]. Climate model projections broadly reinforce this heterogeneous picture. Many regions are expected to experience intensification of heavy precipitation even where mean precipitation declines, particularly in Mediterranean and semi-arid climates[15,34–36].

Beyond changes in mean and extreme precipitation considered separately, observational evidence indicates a systematic shift in how annual precipitation is distributed over time. Globally, the fraction of annual rainfall contributed by very heavy events has increased over the twentieth century[3,37], indicating that precipitation is increasingly delivered through a smaller number of intense events. This tendency is consistent with climate projections and IPCC assessments attributing widespread intensification of heavy precipitation primarily to anthropogenic warming, while emphasizing regional variability in magnitude and direction of change[35].

Despite growing recognition of these changes, most studies continue to analyze total precipitation and precipitation extremes as separate metrics. Analyzing these components independently can obscure an important structural shift in precipitation regimes. In many regions, an increasing share of annual precipitation is delivered during a small number of intense events. Such temporal concentration of rainfall has important hydrological implications, including amplified flood peaks, reduced soil moisture retention, and limited groundwater recharge[34,35,38–43]. For example, in parts of the Mediterranean, a single day's rainfall can account for more than half of winter precipitation[12,44,45]. Conversely, decreases in total precipitation can amplify the relative contribution of extreme events even if those extremes do not intensify, highlighting the need to interpret precipitation extremes in relation to annual totals rather than in isolation.

To address this gap, we present a global-scale assessment of changes in the relationship between extreme and total precipitation using the Extreme Precipitation Fraction (EPF), defined as the ratio of the annual maximum daily precipitation to total annual precipitation. This metric captures the temporal concentration of precipitation—i.e., the extent to which a larger fraction of annual rainfall is delivered by fewer, more intense events. This provides a measure of event dominance within annual precipitation totals, complementing percentile- and wet-day-based metrics by explicitly linking extremes to total rainfall.

We analyze historical patterns and future trends in EPF across a multi-model ensemble of 25 CMIP6 simulations and quantify how changes in annual maximum daily precipitation and total annual precipitation individually contribute to EPF trends using a first-order relative-change decomposition. This framework allows us to distinguish whether increasing EPF reflects intensifying extremes, declining background rainfall, or a combination of both. The following sections present the results, including historical evaluation, projected trends, robustness and agreement analyses, and trend decomposition (Sect. 2), followed by interpretation of hydroclimatic implications across climate regimes (Sect. 3) and concluding with key implications for water management under climate change (Sect. 4).

Results

We investigate spatial and climatic variations in precipitation characteristics by analyzing three metrics: (1) mean fraction of annual precipitation contributed by the single largest daily event—referred to here as the Extreme Precipitation Fraction (EPF), (2) trends in the EPF, and (3) the relative contributions of changes in extremes and changes in total annual precipitation to observed EPF trends. To better understand the relative contributions of these shifts, we decompose the EPF trend into two components: one attributed to changes in the extreme precipitation values and one to changes in total annual precipitation. The analysis is conducted at the grid-cell level using an ensemble of global climate models (GCMs), and results are aggregated by Köppen-Geiger climate classifications to enable a climate-based synthesis.

We start by examining the historical distribution and variability of Extreme Precipitation Fractions (EPFs). Given that the frequency, intensity, and temporal structure of precipitation extremes differ across climatic regimes, we assess EPF across Köppen-Geiger (KG) climate zones, continents, and latitudinal bands to capture global hydroclimatic diversity (see KG climate map in Fig. S1 of the Supplement).

Figure 1 presents an overview of EPF patterns during the historical period (1980–2014), derived from the multi-model ensemble of CMIP6 NASA NEX-GDDP simulations. The spatial map and climate-class ranking highlight pronounced differences across regions. The highest mean EPF values are observed in hot desert (BWh) and cold desert (BWk) zones, with averages of 0.153 and 0.139, respectively. Semi-arid steppe climates (BSh and BSk) also show elevated EPF values (~ 0.089–0.090), reflecting the episodic nature of rainfall in drylands.

Polar climates show more moderate EPF values relative to deserts and steppes. Polar climates such as ice cap (EF) display EPF values of 0.084. The latitudinal distribution highlights pronounced EPF maxima in the subtropical dry belts (approximately 20°–35° N/S). EPF peaks in both the Northern and Southern Hemisphere subtropics; however, the Northern Hemisphere maximum is stronger, reflecting the extensive dryland regions of North Africa, the Middle East, and Central Asia. Continental averages range from 0.048 in Europe to 0.175 in Africa, with Oceania (0.105) and Asia (0.098) also showing relatively high values. Standard deviation map (Fig. 1e) and histograms indicate greater inter-model spread in transition zones—particularly parts of South America, Central Asia, and subtropical Africa.

To evaluate the ability of CMIP6/NEX-GDDP models to reproduce the observed relationship between extreme and annual precipitation, we validate historical EPF values against the Princeton Global Forcing dataset for 1961–2014 as shown in Fig. 2. The ensemble exhibits strong agreement with observations, with a near-zero global mean bias and most land grid cells falling within a narrow ± 0.05 EPF bias range. The spatial

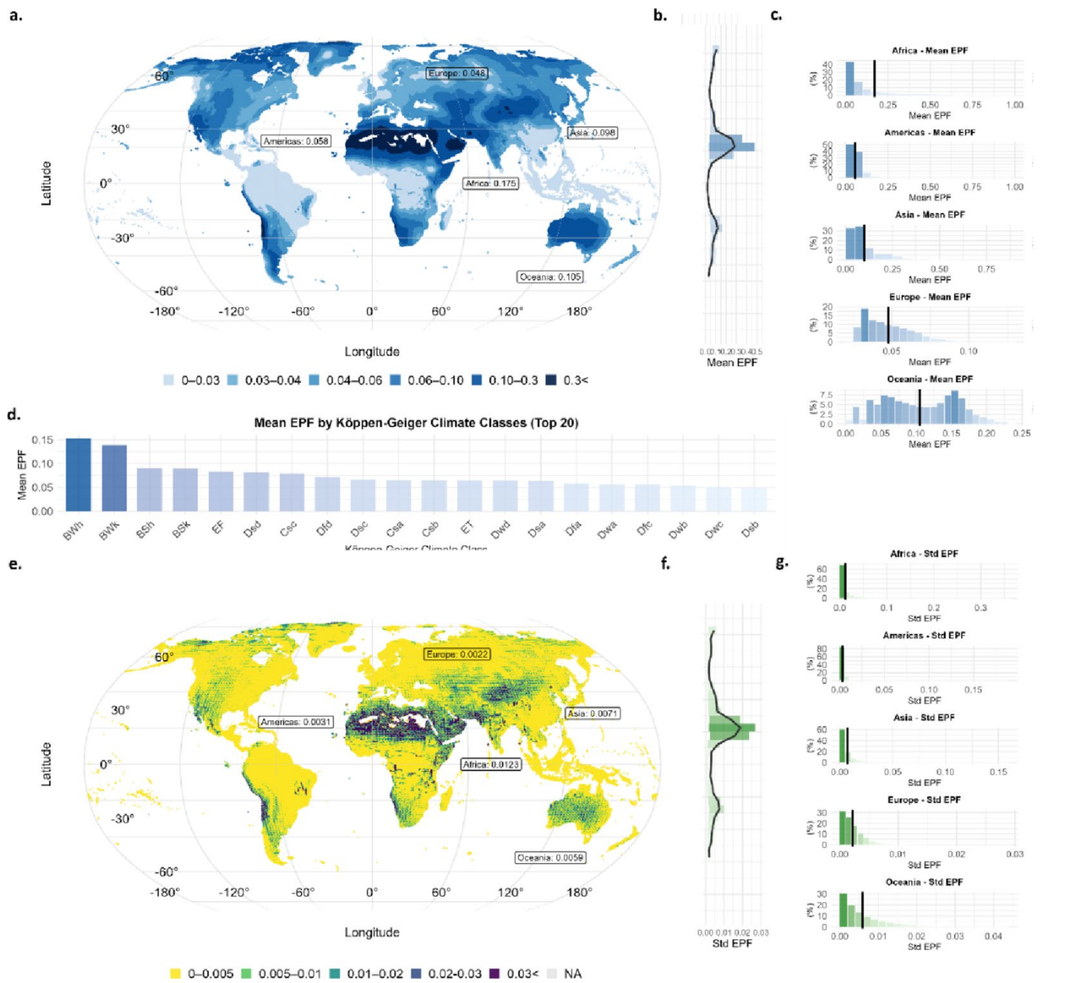

Fig. 1. The spatial and latitudinal distribution of the Extreme Precipitation Fraction (EPF) during the historical period (1980–2014), based on multi-model means from CMIP6 NASA NEX-GDDP simulations. Panel (**a**) shows the global spatial distribution of mean EPF values. Panel (**b**) displays a latitudinal histogram of mean EPF values. Panel (**c**) presents a histogram of mean EPF values across five continents, annotated with continental averages. Panel (**d**) shows a ranked bar plot of the top 20 Köppen-Geiger climate classes based on their mean EPF values. Panel (**e**) maps the spatial standard deviation of EPF across models for each grid cell, highlighting areas of greater inter-model variation. Panel (**f**) presents a latitudinal histogram of EPF standard deviation. Panel (**g**) displays a histogram of EPF standard deviation across continents, showing the distribution and average variability within each region. Maps were generated using Python 3.11 (https://www.python.org/).

distribution of mean error shows that model performance is particularly robust across mid-latitude regions of North America, Europe, and large parts of Asia, while the largest discrepancies occur over subtropical–tropical Africa and high-latitude Arctic regions, where precipitation processes are known to be more challenging for global climate models[46–48]. Additional discrepancies are apparent in regions of strong convective activity and complex topography, consistent with previously documented limitations in simulating precipitation intensity and variability[49,50]. Zonal averages further reveal that the ensemble accurately captures the observed latitudinal structure of EPF across tropical, subtropical, and midlatitude belts, with deviations increasing only toward the highest northern latitudes. Climate-zone evaluation confirms that a large majority of Köppen–Geiger climate classes exhibit high consistency between modeled and observed EPF, with most grid cells lying within the inter-model range.

To assess how the structure of annual rainfall is evolving under climate change, we analyze trends in EPF under the high-emissions SSP585 scenario shown in Fig. 3. All EPF trends are expressed as percentage change per decade (% per decade). The global signal reveals a pronounced tendency toward more extreme-dominated precipitation regimes, particularly across dryland and Mediterranean-type climates. The strongest increases are projected in cold deserts (BWk: +0.26), while Mediterranean climates (Csa, Csb, Csc) consistently rank among the top intensifying classes, with trends exceeding + 0.20.

In contrast, polar and high-latitude snow-dominated zones show declining EPF trends. The steepest decreases occur in tundra (ET: − 0.14), ice cap (EF: − 0.13), and subarctic snow-dominated climates such as Dfd (−0.13) and Dsd (−0.16).

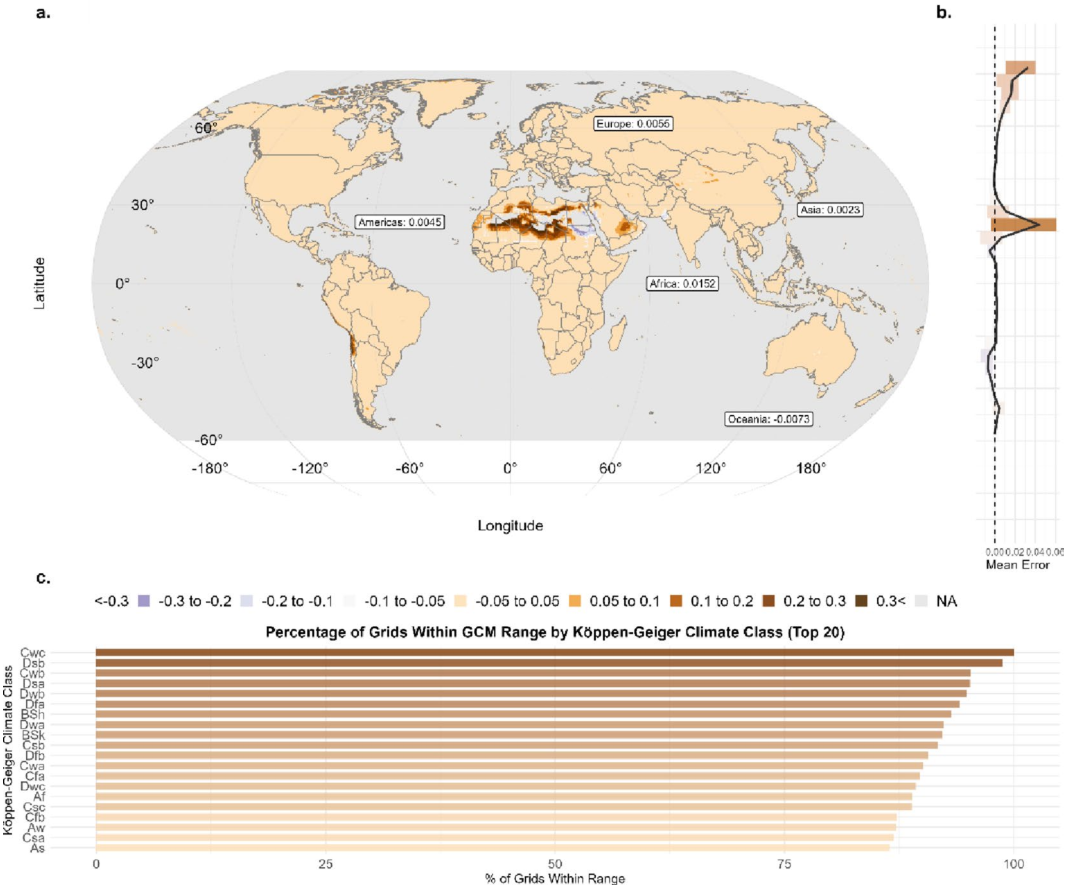

Fig. 2. Historical EPF Mean Error. Panel (**a**) shows spatial distribution of mean error (ME) between CMIP6/NEX-GDDP ensemble-mean EPF values and EPF computed from the Princeton Global Forcing dataset (1961–2014), with boxes presenting continental mean ME values. Colored points show ME at each land grid cell. Panel (**b**) depicts zonal mean, median, 25th, and 75th percentiles of ME, illustrating the latitudinal structure of model skill. Panel (**c**) summarizes the percentage of grid cells within the observational range across Köppen–Geiger climate classes. The map was generated using Python 3.11 (https://www.python.org/).

The latitudinal distribution of EPF trends shows a clear meridional pattern, with negative trends dominating high northern latitudes and positive trends concentrated in the subtropical dry belts of both hemispheres. These latitude bands correspond to major desert belts and Mediterranean-type climates. Continental mean EPF trends further summarize this spatial variability. Oceania shows the largest mean increase (+0.15), followed by Africa (+0.055), while the Americas, Asia, and Europe exhibit near-zero or slightly negative mean trends. A similar analysis under the SSP245 scenario is provided in Fig. S2.

To assess whether EPF trends reflect broader changes in the upper tail of the precipitation distribution, we examined trends in the contribution of the wettest 1% of daily precipitation (Top-1%) as shown in Fig. 4. Under SSP585, Top-1% contributions increase across large portions of the globe. Strong positive trends are particularly evident in Mediterranean and temperate dry-summer climates (Csa, Csb), where mean increases reach approximately 0.7–0.8% per decade, as well as in cold-arid and semi-arid regions (e.g., BWk), where mean increases exceed 0.6% per decade.

In contrast, pronounced negative trends in the Top-1% contribution are concentrated in high-latitude and polar climates, including ET, EF, Dfd, and Dsd classes, with mean declines on the order of −0.45 to −0.55% per decade. These patterns indicate that reductions in upper-tail contributions are largely limited to cold regions, whereas lower-latitude regions more frequently exhibit stable or increasing values. Overall, the spatial distribution of Top-1% trends mirrors the heterogeneity of EPF changes under SSP585. Comparable but weaker and more noisy patterns are found for SSP245 as shown in Fig. S3, while corresponding analyses for the Top-5% metric under both scenarios are presented in the Supplementary Information (Figs. S4 and S5).

To address robustness and inter-model consistency, we next summarize EPF changes using a robust trend classification that combines field significance (FDR-adjusted $p < 0.05$) with agreement in the sign of change across the CMIP6 ensemble (≥60% of models). The results for SSP585 are shown in Fig. 5. Robust EPF increases occur across substantial portions of land areas in several climate regimes, reaching approximately 10–30% of grid cells within many warm continental, monsoonal, and semi-arid Köppen–Geiger classes (e.g., Dwa, Dwb, Dfa, BSk, and BWh).

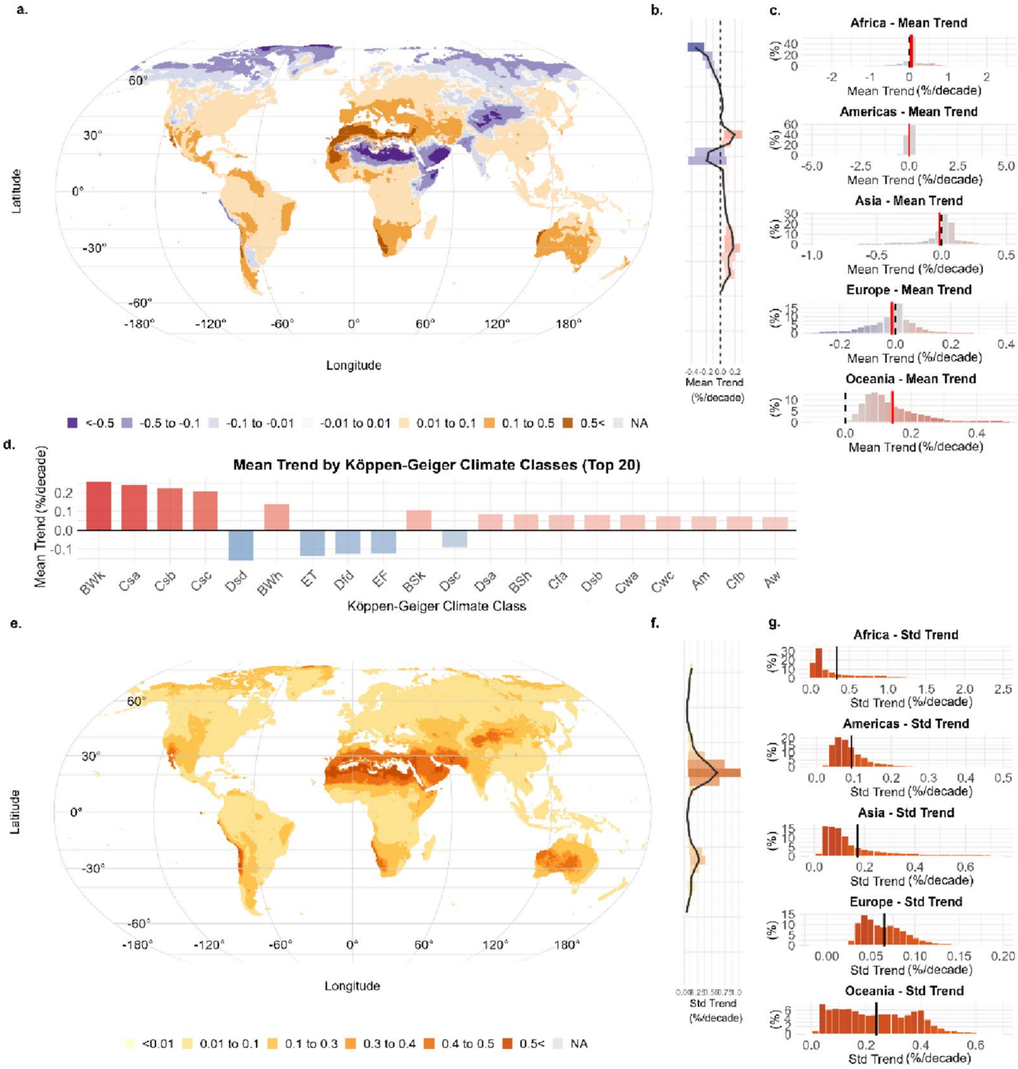

Fig. 3. The spatial and latitudinal distribution of trends in the EPF under the SSP585 scenario (2015–2100), based on multi-model ensemble-mean Sen slopes computed across all land grid cells from CMIP6 NASA NEX-GDDP simulations. EPF trends represent the rate of change in the share of annual precipitation falling in the single wettest day of the year (% per decade). Panel (**a**) shows the global spatial distribution of ensemble-mean EPF trends at each grid cell. Panel (**b**) displays a latitudinal histogram of ensemble-mean EPF trends aggregated across all grid cells within each latitude band. Panel (**c**) presents a histogram of EPF trends across five continents, annotated with continental averages. Panel (**d**) shows a ranked bar plot of the top 20 Köppen-Geiger climate classes based on their mean EPF trend computed across all land grid cells within each class. Panel (**e**) maps the spatial standard deviation of EPF trends across models for each grid cell, identifying areas of elevated inter-model spread. Panel (**f**) presents a latitudinal histogram of EPF trend standard deviation. Panel (**g**) displays a histogram of EPF trend standard deviation across continents, highlighting regional differences in uncertainty. Statistical significance and robustness of EPF trends—based on FDR-adjusted Mann–Kendall tests and inter-model agreement—are assessed separately and presented in Fig. 5. Maps were generated using Python 3.11 (https://www.python.org/).

EPF increases are concentrated in mid-latitude and subtropical regions, where approximately 20% of grid cells within several climate classes exhibit statistically significant and model-consistent increases. Across the same classes, 30–55% of grid cells exhibit FDR-significant ensemble-mean EPF trends under SSP585. In contrast, robust EPF decreases primarily occur in high-latitude cold climates (e.g., Dfc, Dwc, Dsc, and Dfd), where 5–20% of grid cells show model-consistent declines. A corresponding robustness assessment for SSP245 (Fig. S6) shows similar spatial patterns but reduced spatial coverage, consistent with weaker forcing.

To provide a more nuanced understanding of climate change impacts on precipitation extremes beyond zonal averages, we analyzed the full distribution of EPF slopes pooled across all grid cells and all contributing CMIP6 GCMs within each Köppen–Geiger (KG) climate class. Figure 6 presents the probability density functions of the EPF trend slopes for each Köppen-Geiger class, highlighting both the central tendency and dispersion of slope values arising from joint spatial heterogeneity and inter-model variability. Mediterranean climates

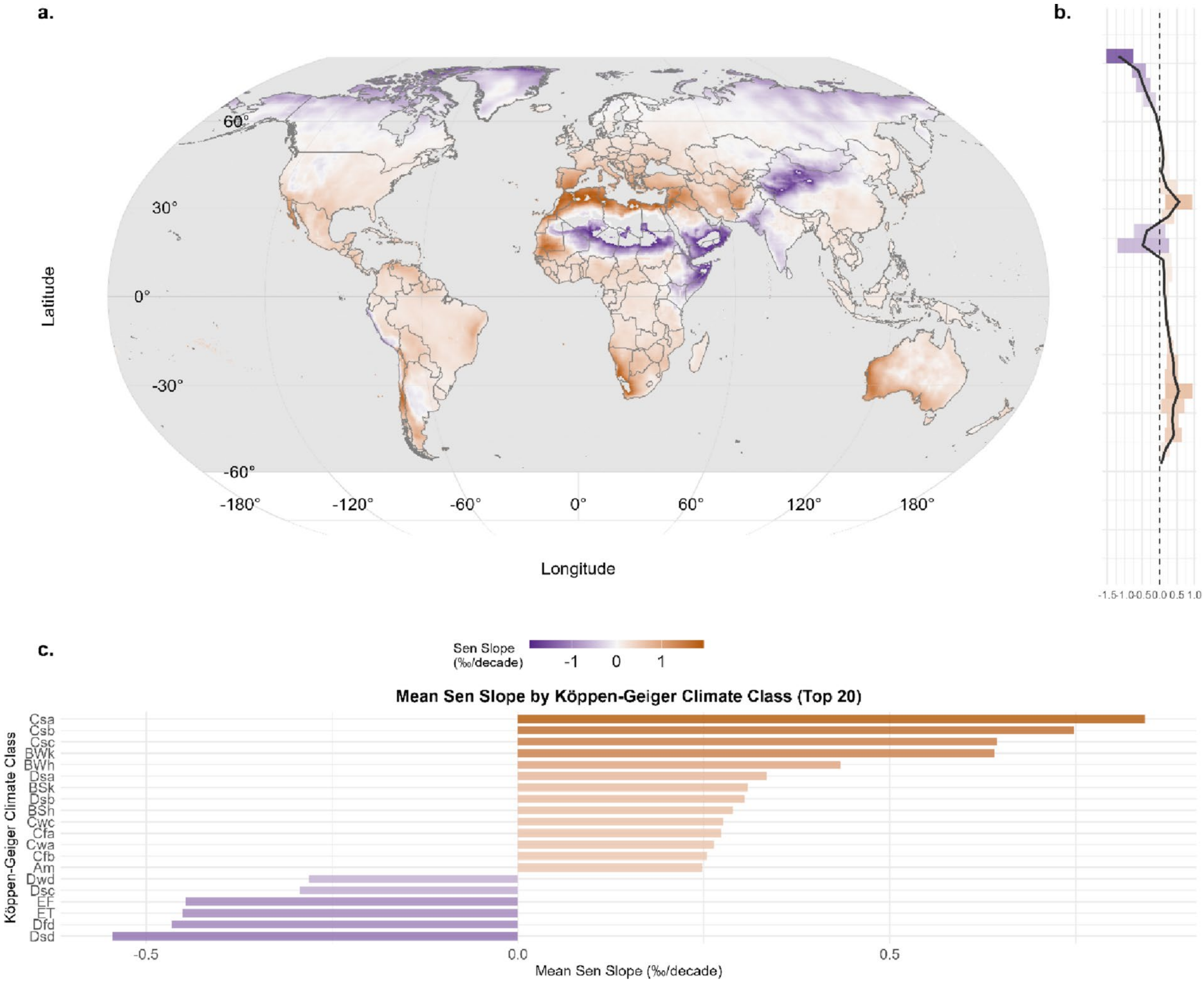

Fig. 4. Ensemble trend direction of Top-1% precipitation contribution under SSP585. Panel (**a**) shows global spatial distribution of the ensemble-mean Sen slope (% per decade) for the fraction of annual precipitation contributed by events exceeding the 99th percentile. Colors indicate the direction and magnitude of trends, with warm colors denoting increasing contributions from the most extreme events and cool colors indicating decreasing contributions. Panel (**b**) shows the zonal (latitudinal) mean profile, while panel (**c**) summarizes mean trends across Köppen–Geiger climate classes (top 20 by absolute magnitude). Results highlight increases in Mediterranean and semi-arid climates and decreases in high-latitude and polar regions. Corresponding analyses for SSP245 and for the Top-5% metric are provided in the Supplementary Information. The map was generated using Python 3.11 (https://www.python.org/).

with dry summers (Csa, Csb, and Csc) exhibit among the highest average EPF trends, with mean slopes of approximately + 0.24, + 0.17, and + 0.21, respectively, and more than 70% of grid–model realizations in these zones experiencing increases greater than + 0.1. This strong upward shift in EPF slopes is not only evident in the mean but also in the heavy positive tail of their distributions, with 95th percentile values reaching as high as + 0.7. The results under the SSP245 scenario are presented in Fig. S7.

In contrast, semi-arid and continental climates such as BSk and Dsb show more moderate mean slopes (+ 0.09 to + 0.1) but still display considerable spread, with up to 45–50% of grid–model slope estimates showing positive slope values above + 0.1. Oceanic temperate zones like Cfb and high-elevation subtropical types like Cwc also exhibit positive mean slopes, though with more symmetric and narrowly centered distributions. Meanwhile, tropical and polar classes (e.g., Am, Af, ET, EF) show smaller mean trends and narrower density shapes. These distributions show that positive EPF trends are widespread within several climate classes. They also highlight spatial variability in EPF trends, particularly in arid and Mediterranean zones, which may be linked to local topographic, convective, or land-use dynamics.

To interpret EPF trends in terms of their contributing components, Fig. 7 decomposes the EPF trends into their constituent terms: the relative (percentage) changes in annual maximum daily precipitation and total annual precipitation. This decomposition reveals distinct spatial and climatic regimes. In tropical rainforest climates (Af), the contributions of annual maximum and total precipitation are nearly balanced—around 54% and 46%, respectively. In temperate humid zones (Cfa), the annual maximum daily precipitation dominates,

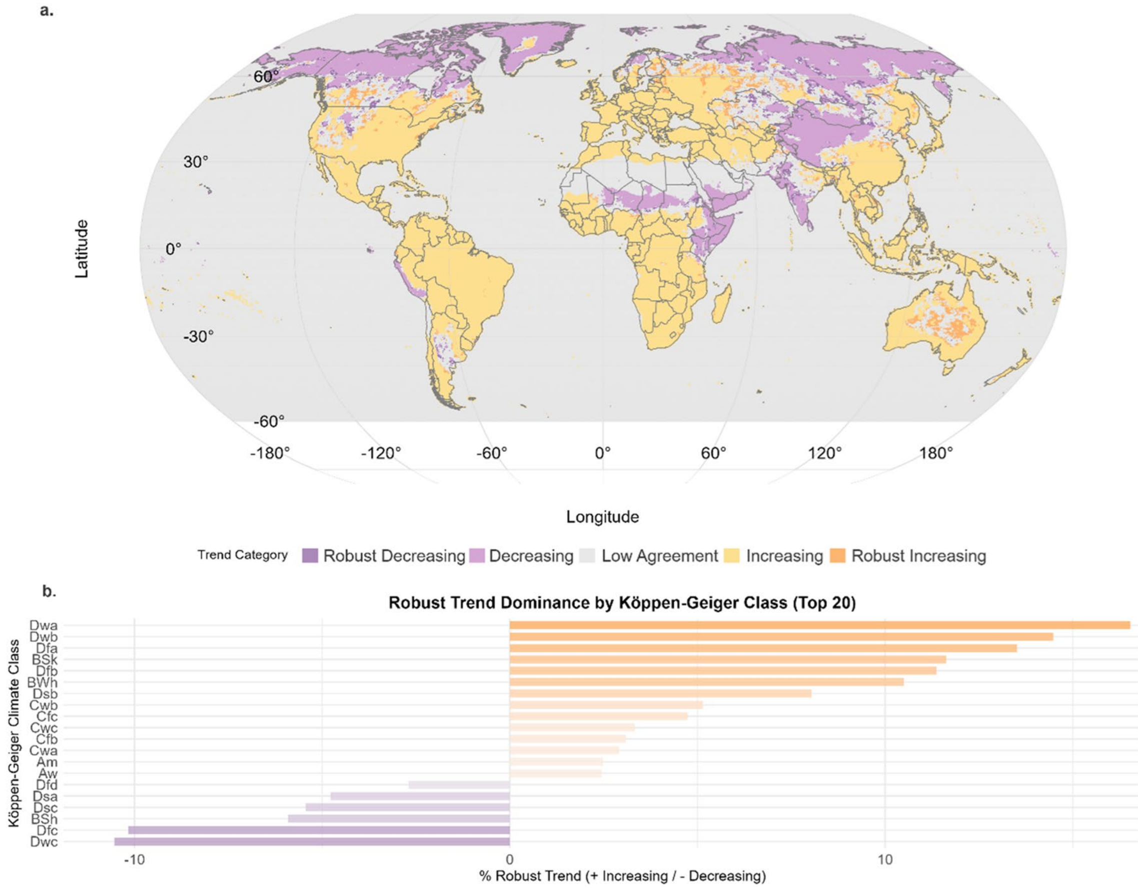

Fig. 5. Robustness of projected EPF trends under SSP585. Panel (**a**) shows global map classifying EPF trend behavior by combining (i) field-significant ensemble-mean trends (FDR-adjusted $p < 0.05$) and (ii) inter-model agreement in the sign of change (≥ 60% of CMIP6 models). Categories indicate robust increases/decreases (significant + agreement), increases/decreases with agreement but not field-significant, and low-agreement regions. Panel (**b**) summarizes dominance of robust changes across Köppen–Geiger climate classes. An analogous robustness analysis for SSP245, using the same criteria, is provided in Fig. S6. The map was generated using Python 3.11 (https://www.python.org/).

contributing 55% on average to EPF changes—the highest among all climate classes—while similar contributions are observed in Dwa (54%) and Cwa (52%).

In contrast, arid and semi-arid regions such as hot and cold deserts (BWh, BWk) and cold steppe (BSk) show that EPF changes are primarily dominated by changes in total annual precipitation, with the contribution of the annual maximum ~ 40%. Mediterranean climates (Csa–Csc) show an even stronger dominance of total precipitation, where contributions from the annual maximum average around 38–44%, and the influence of total rainfall exceeds 55–60%.

These patterns are reflected in the latitudinal breakdown. Equatorial latitudes (2.5°S to 2.5°N) show near-equal contributions (annual maximum: 53–55%), while mid-latitudes show a greater imbalance between the contributions of the annual maximum and total precipitation. For example, at 37.5°N, the annual maximum contribution is ~ 43%, and total precipitation accounts for ~ 57%. Notably, higher latitudes (> 67.5°N) exhibit a consistent decline in annual maximum influence, dropping from 37% at 67.5°N to only 27% at 82.5°N, indicating that in polar regions, EPF trends are overwhelmingly shaped by total precipitation changes, possibly due to transitions from snow to rain and reduced seasonality. These patterns highlight that EPF increases do not imply intensification of extremes per se, but rather reflect cases where the annual maximum changes more rapidly (or less slowly) than the annual total.

At the continental scale, the contribution of annual maximum precipitation remains below 45% on average, with Oceania showing the highest (43.4%) and Africa the lowest (40.1%). In polar regions (ET, EF) and snow-dominated zones (e.g., Dfc, Dfd), both components contribute relatively equally, typically showing a 44–56% split, reflecting broader shifts in the precipitation regime—likely related to snow-to-rain transitions and changes in seasonality. These findings underscore the spatial heterogeneity in the contribution of annual maxima and total precipitation in changing EPF trends: while intensification of daily extremes is the primary contributor in many humid and temperate regions, changes in total annual precipitation dominate in arid, Mediterranean, and high-latitude environments. Analogous results under the SSP245 are presented in Fig. S8.

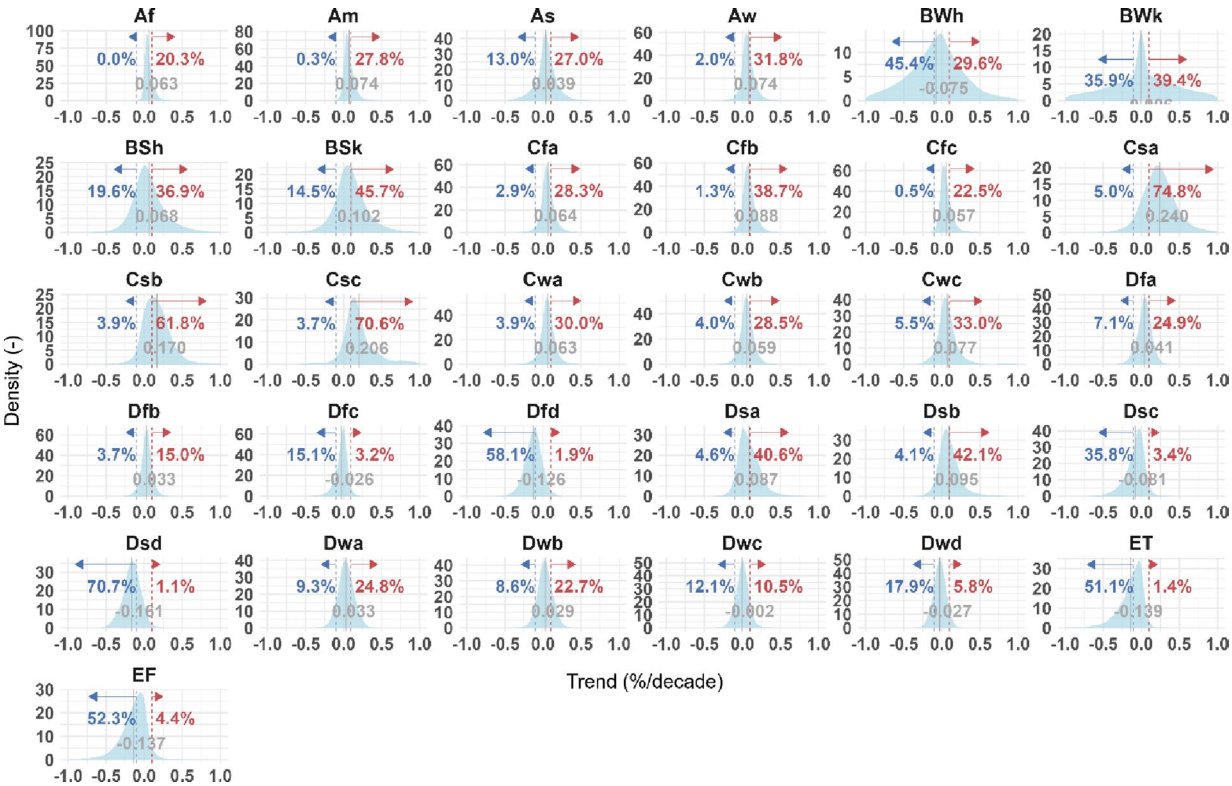

Fig. 6. Probability distributions of EPF trend (ssp585) across Köppen-Geiger climate classes. Each panel shows the kernel density estimate of grid-level EPF slopes pooled across all grid cells and CMIP6 models belonging to a given climate class. Vertical dashed lines at ± 0.1 denote moderate positive and negative trends, and vertical solid lines indicate class means. Arrows and percentage labels indicate the proportion of grid cells with slopes greater than + 0.1 (red) and less than − 0.1 (blue), offering a view into the spatial dominance of extreme trends within each climate regime.

Discussion

The results indicate that extreme precipitation fraction (EPF) is changing unevenly across different climate regions. This spatial variability is consistent with hydrological intensification under warming, which enhances the potential for stronger precipitation extremes but manifests differently depending on regional climate regimes and the relative responses of total versus extreme precipitation[3,8,17,35]. Rather than uniform increases, EPF responses exhibit strong regional structure, reflecting differences in baseline climate, precipitation regimes, and the relative behavior of extreme versus total precipitation[3,14–52].

The historical validation exercise further reinforces the credibility of these projected EPF changes. By comparing CMIP6/NEX-GDDP simulations against the Princeton observational dataset, we show that the models reproduce the observed spatial distribution, latitudinal structure, and climatic-region patterns of EPF during the historical period. The small global mean bias, the high proportion of grid cells falling within observational bounds, and the strong agreement across continents collectively demonstrate that the ensemble captures the fundamental balance between extreme precipitation and total annual rainfall. This supports the credibility of the projected EPF patterns discussed below. Observational records already show upward trends in extreme precipitation in many regions over recent decades, including northern Europe, North America, parts of Asia, and the Mediterranean[13,42,53–55]. As a consequence, the "when it rains, it pours" phenomenon is expected to become more pronounced globally, raising important implications for floods, droughts, and water management[23,37,43,56–59].

While the global trend is toward a higher fraction of rain falling in extreme events, the magnitude and reasons for these changes vary by climate. The analysis highlights especially strong or noteworthy changes in arid, polar, and Mediterranean zones. Arid regions receive very low total precipitation, but often in short, intense bursts (e.g., rare heavy rain in deserts). Our results reveal a consistent pattern across dryland regions, with both semi-arid steppe climates (BSh, BSk) and hyper-arid desert climates (BWh, BWk) showing clear increases in EPF. These patterns can be interpreted through changes in moisture availability. Warming temperatures allow the atmosphere to hold more water vapor, so when precipitation does occur in dry regions, it can be more intense[10,17,60,61]. Even regions that are projected to get drier in terms of mean rainfall can experience heavier individual rainstorms because of thermodynamic increases in moisture capacity (roughly ~ 7% more water vapor per °C of warming)[61]. Indeed, one global study finds all climate regions (including arid zones) show intensification of extreme precipitation by the late 21st century, although the magnitude of increase is larger in wetter regions and smaller in extremely dry regions[17]. Additional influences from circulation changes

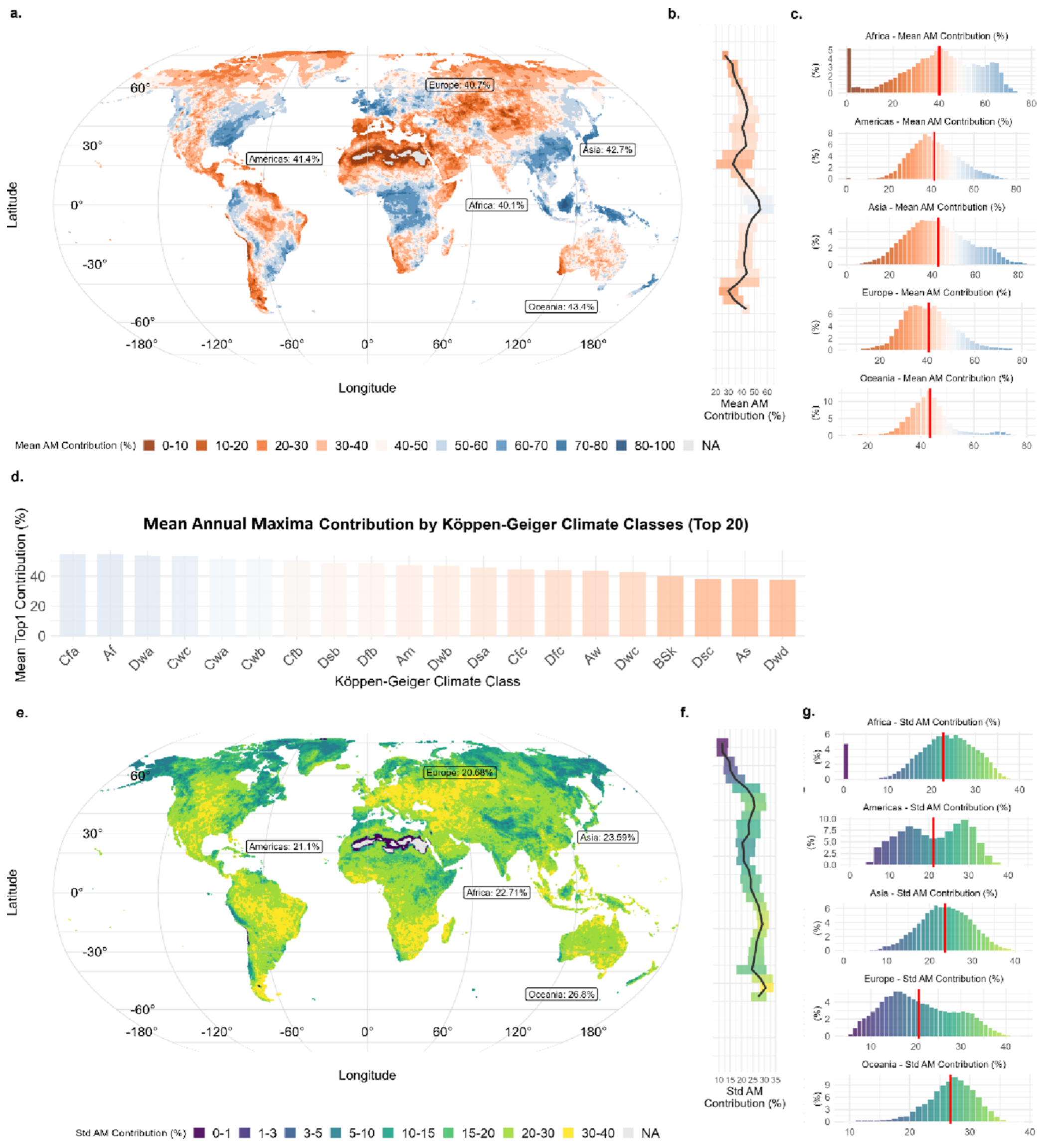

Fig. 7. The spatial and latitudinal distribution of the mean contribution of the annual maximum (AM) daily precipitation to the trend in the Extreme Precipitation Fraction (EPF) under the SSP585 scenario, based on CMIP6 NASA NEX-GDDP multi-model simulations. The contribution is calculated as the percentage of the EPF trend that is attributable to changes in the annual maximum daily precipitation, providing insight into the dominant contributors of intensifying precipitation extremes. Panel (**a**) shows the global spatial distribution of the multi-model mean contribution values. Panel (**b**) displays a latitudinal histogram of these contributions. Panel (**c**) presents the distribution of contribution values across continents, annotated with average percentages. Panel (**d**) ranks the top 20 Köppen-Geiger climate classes by their average contribution values. Panel (**e**) maps the spatial standard deviation of the contribution values across models, illustrating areas of high inter-model spread. Panel (**f**) presents a latitudinal histogram of this standard deviation. Panel (**g**) displays a histogram of standard deviation across continents, summarizing regional uncertainty in the attribution of EPF trends. Maps were generated using Python 3.11 (https://www.python.org/).

may further reduce precipitation frequency while favoring episodic, high-intensity events, contributing to the observed EPF increases.

These shifts have important hydrological implications in dryland regions. Infrequent but intense rainfall events in deserts can trigger destructive flash floods and severe erosion[62–64], while longer dry intervals between events may exacerbate drought conditions. Together, these effects complicate water management in arid and semi-arid environments.

Polar tundra (ET) and ice-cap (EF) regions show some of the most distinctive precipitation shifts under climate change[65,66]. These regions exhibit declining EPF trends, primarily because increases in total annual precipitation outpace changes in annual maximum daily precipitation rather than reflecting a reduction in extreme events themselves. Decomposition results consistently show that positive trends in total precipitation dominate EPF changes at high latitudes, consistent with enhanced moisture transport, increased rain-to-snow ratios, and Arctic amplification[34,35,67–70]. As a result, the contribution of the annual wettest day to total precipitation decreases despite overall wetting.

The largest EPF increases are observed in Mediterranean-type climates, which are characterized by hot, dry summers and wetter winters. Our results show a strong increase in the fraction of rain from extreme events in these regions—among the largest increases of any climate zone. This is consistent with the Mediterranean being a well-known climate change hotspot where mean rainfall is declining but heavy rainfall is intensifying in certain seasons[41]. Climate projections uniformly show that the Mediterranean region will become drier on average, especially in the dry season. Annual precipitation can decrease by around 4% per °C of global warming, with summers seeing pronounced drying[15,42]. This reduction in mean rainfall, combined with higher temperatures, is already increasing drought frequency and severity[42,71–73]. Even as total precipitation drops, extreme precipitation events are expected to become more intense[74,75]. Observations have noted upward trends in heavy precipitation in parts of the northern Mediterranean[42,75], and high-resolution models project further increases in extreme rainfall intensity particularly for rare, high-impact storms[75]. For example, one study found that 50-year return period daily rainfall extremes could double in magnitude across the Mediterranean by late century under business-as-usual emissions[42].

Our EPF results indicate that the contribution of the single wettest day of each year to annual precipitation is projected to rise by 5–28% throughout the Mediterranean region[42]. Such changes substantially increase the risk of flash flooding following prolonged dry periods, while simultaneously exacerbating water scarcity, thereby amplifying hydroclimatic risk[76–79].

Tropical climates and temperate humid (Cfa/Cfb) climates also show rising EPF in our analysis, though less dramatically than the above cases. In tropical rainforest and monsoonal regions, abundant moisture and convective activity mean extreme events are already common; future warming is expected to further intensify peak rainfall rates, often following Clausius–Clapeyron scaling[8,12,35]. However, changes in monsoon circulation or tropical storm frequency can modulate regional patterns[12]. Tropical areas are seeing heavier rainfall extremes, with observed increases in short-duration intensities and projections of more high-percentile rainfall as the climate warms[12,14]. These trends are expected to continue in future, linked to more frequent atmospheric moisture convergence and slow-moving storm systems in warmer climate[33,80–83]. One notable pattern in cold continental (D) climates is that the most extremely continental winter regions (e.g., subarctic interiors with very cold winters, Dfd/Dwd) showed a decrease in EPF in our analysis. These EPF declines are comparable to those observed in polar regions and reflect increases in total annual precipitation relative to changes in annual maximum daily precipitation[34,67,84]. In contrast, continental regions with pronounced wet seasons or storm activity (e.g., monsoonal or Mediterranean-influenced Dsa/Dsb climates) see EPF increases. These nuances illustrate that the response of precipitation extremes is an interplay of thermodynamics (which tends to universally increase moisture and extremes) and regional atmospheric dynamics (which can redistribute when and how rain falls)[8,24,33].

Uncertainty remains an inherent component of regional climate projections, particularly in convective regions, areas of complex topography, and climate transition zones. To address this, the analysis combines bias-corrected CMIP6 simulations with ensemble-based robustness diagnostics, including inter-model agreement and field-significant trend detection. This approach distinguishes coherent large-scale EPF signals from regions with high model disagreement. Despite local uncertainty, the consistent emergence of EPF increases in arid, semi-arid, and Mediterranean climates, and decreases at high latitudes across multiple models and diagnostics, indicates that the broad spatial patterns identified here are robust. Future work using convection-permitting and regional climate models will help refine EPF estimates at finer spatial scales and improve understanding of local precipitation processes.

Conclusion

Our global assessment of the Extreme Precipitation Fraction (EPF) reveals that climate change is driving a substantial change in precipitation regimes, with important hydrological implications. Using a decomposition framework applied to a multi-model ensemble of CMIP6 simulations, we demonstrate that EPF trends—and their underlying contributors—vary markedly across climate zones. The strongest increases in EPF are projected for arid, semi-arid, and Mediterranean climates, where declining total precipitation amplifies the fractional dominance of extreme events. In contrast, changes in extremes are primarily associated with EPF increases in many temperate and tropical regions. Meanwhile, polar climates are projected to experience decreasing EPF, reflecting increases in total annual precipitation that outpace changes in annual maximum daily precipitation, thereby reducing the relative contribution of the wettest day to the annual total.

The evolving patterns of EPF have profound hydrological consequences. In dryland regions, increasing reliance on a few intense rain events heightens flash flood risks while deepening drought vulnerability between events. In Mediterranean zones, the co-occurrence of drying trends and more concentrated rainfall threatens both water supply and flood resilience. In temperate and tropical regions, intensifying extremes will challenge the capacity of water infrastructure and demand adaptive management. Conversely, polar regions face rapid shifts in precipitation phase and seasonality, with potential disruptions to snowmelt-driven hydrology.

Our findings underscore the importance of moving beyond traditional metrics of mean precipitation or extreme event frequency alone. EPF provides a physically meaningful lens through which to assess the emerging structure of rainfall under climate change. By explicitly linking extremes to total precipitation, this metric highlights new forms of hydroclimatic risk that will increasingly shape water management challenges in a warming world. Future work should further refine EPF-based metrics for operational use, explore their variability at sub-seasonal timescales, and integrate them with impact-oriented hydrological models to better inform adaptation strategies.

Data and methods
Data
This study utilizes daily precipitation projections from the NASA NEX-GDDP-CMIP6 dataset[85], which provides bias-corrected simulations of global climate model (GCM) outputs from the Coupled Model Intercomparison Project Phase 6 (CMIP6) archive[86]. The NEX-GDDP-CMIP6 product applies the BCSD (Bias-Correction Spatial Disaggregation) method to correct systematic biases in CMIP6 outputs and downscale them to a 0.25° spatial resolution (~ 25 km), thereby enabling high-resolution impact assessments. The dataset spans the historical period (1950–2014) and future projections (2015–2100) under four shared socioeconomic pathways (SSPs).

We analyze simulations from 25 GCMs (one run per GCM) for which daily precipitation data were available in the NEX-GDDP-CMIP6 archive. The complete list of models is provided in Appendix Table S1 in the Supplement. We selected the NASA NEX-GDDP-CMIP6 dataset for this analysis as it provides globally consistent, bias-corrected, and spatially downscaled daily precipitation data, which are essential for robust estimation of precipitation extremes and their contribution to trends. NEX-GDDP-CMIP6 corrects model biases relative to observations and improves the representation of both mean and extreme precipitation statistics at local scales[85,87]. The higher spatial resolution (0.25°) and bias correction make NEX-GDDP particularly suitable for calculating metrics such as the Extreme Precipitation Fraction (EPF), which are sensitive to the accuracy of daily precipitation extremes. Furthermore, NEX-GDDP is widely used in hydrological and climate impact assessments[88–92], and provides a consistent, publicly available dataset across multiple GCMs, facilitating inter-model comparison and robust ensemble statistics.

Climate regimes are defined using the global Köppen–Geiger climate classification of Beck et al. (2018)[93], derived from observed temperature and precipitation climatologies and available at 1-km spatial resolution.

In regions characterized by extremely low or near-zero precipitation (e.g., hyper-arid deserts), daily precipitation values can be zero or undefined for extended periods, leading to missing (NA) values in derived precipitation metrics such as EPF and upper-tail contribution indices. These NA values reflect physically implausible or undefined metric calculations rather than data errors and are treated consistently across all models.

Bias correction of CMIP6 precipitation in NEX-GDDP
The CMIP6 simulations used in this study are obtained from the NASA NEX-GDDP dataset, which applies a quantile-mapping bias-correction approach to daily precipitation. Bias correction is performed separately for each calendar month by mapping the modeled historical precipitation distribution to the corresponding observational distribution, while preserving the rank structure of the modelled data. This method adjusts both light and heavy precipitation values in a distribution-consistent manner and is designed to correct systematic biases without modifying the long-term climate change signal or altering model-simulated trends. Because quantile mapping is applied to the entire precipitation distribution, both total annual precipitation and annual maximum daily precipitation are corrected using the same transformation function, ensuring physical consistency between the components of the EPF metric. Previous evaluations of NEX-GDDP have shown that this procedure preserves relative changes in means and extremes and does not artificially inflate or suppress projected trends.

To verify that bias correction does not distort EPF behavior, we compare bias-corrected CMIP6 EPF values against observations from the Princeton Global Meteorological Forcing Dataset (GMFD) dataset[94,95]. GMFD is a globally gridded, observation-based meteorological forcing dataset derived from a combination of station observations, satellite products, and reanalysis data, providing daily precipitation at 0.25° spatial resolution over land areas for the period 1948–2014. The dataset has been widely used for hydrological modeling, land-surface simulations, and climate model evaluation, and is commonly treated as a benchmark observational reference for global precipitation analyses. Using PGF daily precipitation, we compute EPF over the historical period and assess the ability of the NEX-GDDP ensemble to reproduce observed spatial patterns, latitudinal structure, and climate-regime variability of EPF.

Methodology
Extreme Precipitation Fraction (EPF)
To characterize the dominance of extreme precipitation events within the annual precipitation regime, we compute the Extreme Precipitation Fraction (EPF), following the approach of Papalexiou and Montanari (2019)[3] and similar recent studies[9]. For each grid cell and year, EPF is defined as:

$$\mathrm{EPF}_y = \frac{P_y^{\max}}{P_y^{\mathrm{tot}}} \tag{1}$$

where $P_y^{\max}$ is the maximum daily precipitation in year y, and P_y^{tot} is the total annual precipitation for that year. EPF thus provides a dimensionless measure (between 0 and 1) of the temporal concentration of annual precipitation into a single extreme event.

In addition to EPF, we analyze two complementary percentile-based indicators that describe how much of the annual precipitation is contributed by very rare but influential events. The first is the Top-1% metric, defined as the fraction of total annual precipitation contributed by days exceeding the 99th percentile of the annual daily distribution. The second is the Top-5% metric, defined analogously for days exceeding the 95th percentile. Together, EPF, Top-1%, and Top-5% characterize different aspects of the tail behaviour of precipitation and allow a more comprehensive assessment of changes in extreme precipitation dominance. Accordingly, EPF is not interpreted here as a standalone indicator of rainfall concentration, but as a descriptive measure of how annual precipitation is partitioned between the single largest daily event and the annual total. Its interpretation is therefore explicitly supported by decomposition into changes in annual maximum precipitation and total annual precipitation, as well as by comparison with complementary upper-tail metrics (Top-1% and Top-5%). Throughout the analysis, EPF trends are examined jointly with changes in annual maximum precipitation, total annual precipitation, and broader upper-tail contributions (Top-1% and Top-5%).

Trend analysis

To assess long-term changes in EPF and its related extreme-precipitation metrics, we applied trend detection procedures to three diagnostic indicators derived from CMIP6 simulations: (1) EPF, (2) the contribution of precipitation events exceeding the 99th percentile of the annual distribution (Top-1% metric), and (3) the contribution of events exceeding the 95th percentile (Top-5% metric). All trend analyses are performed on the bias-corrected NEX-GDDP precipitation data described in Sect. 5.2. Trend estimation was performed independently for each grid cell, each CMIP6 model, and each emissions scenario.

We conduct a Mann–Kendall trend test[96,97] at each grid point to evaluate the statistical significance of monotonic trends. The Mann–Kendall test is a non-parametric method widely used for trend detection in hydroclimatic time series, as it does not assume normality or linearity and is robust to outliers[98].

For grid cells where a statistically significant trend ($p < 0.05$) is detected, we compute the Sen's slope estimator[99] to quantify the magnitude of the trend. Sen's slope calculates the median slope of all pairwise differences in values over time:

$$\beta = \text{median}\left(\frac{X_j - X_i}{j - i}\right), \forall\ j > i \tag{2}$$

where X denotes EPF, Top-1%, or Top-5% values.

Trend estimation is performed for all grid cells regardless of statistical significance; significance testing is used solely to classify trends as significant or non-significant, not to determine whether slopes are computed.

The Mann–Kendall test was applied using two complementary approaches. First, trend estimation was performed independently for each CMIP6 model and each grid cell, enabling quantification of model-specific trends and providing the basis for assessing inter-model agreement. Second, for each grid cell we constructed an ensemble-mean time series by averaging across models using available (non-missing) values, and we applied the MK test to this ensemble-mean series. This ensemble-level trend represents the multi-model forced response. Because trend testing is conducted across tens of thousands of spatial grid cells, pointwise p-values may yield spurious significance due to multiple testing; therefore, ensemble-mean MK p-values were adjusted using the Benjamini–Hochberg False Discovery Rate (FDR) procedure (Wilks, 2006) to account for field significance. Robustness classifications were subsequently based jointly on ensemble significance and the fraction of models agreeing on trend direction. Only grid cells with an FDR-adjusted $p < 0.05$ were considered statistically significant, and all spatial maps mask non-significant cells accordingly, with the resulting field-significant and robust trend patterns summarized in Fig. S6.

Inter-model trend agreement and robustness assessment

To assess the robustness of projected trends, we evaluate **inter-model agreement in trend direction** using the model-specific slopes obtained from the grid-level trend analysis described above. For each grid cell, we compute the percentage of CMIP6 models exhibiting (i) positive trends, (ii) negative trends, and (iii) statistically significant positive or negative trends.

Building on the ensemble-mean trend and its FDR-adjusted significance, we then classify grid cells following IPCC AR6 conventions, integrating statistical significance and model agreement. Each grid cell is categorized as:

- Robust increase — ≥60% of models show a positive trend and the ensemble-mean trend is significant after FDR correction.
- Robust decrease — ≥60% of models show a negative trend and the ensemble-mean trend is FDR-significant.
- Low agreement — the ensemble-mean trend is FDR-significant, but inter-model sign agreement is < 60%.
- Non-robust — no FDR-significant ensemble-mean trend.

Trend decomposition

To better quantify how the observed EPF trends relate to changes in their constituent quantities, we apply a first-order logarithmic decomposition of relative changes, which expresses variations in EPF as the sum of relative changes in annual maximum daily precipitation and total annual precipitation. This approximation is valid for small fractional changes and provides a straightforward accounting of how changes in each component contribute to the overall EPF trend.

The decomposition is applied independently at each grid cell and for each emissions scenario and is used solely as a descriptive tool to partition the EPF trend into contributions arising from changes in the annual maximum and the annual total. No causal interpretation, feedback, or interaction between components is implied. The resulting component contributions are interpreted alongside the robustness classifications described above.

Starting from the definition:

$$d\ln\text{EPF} = d\ln\left(P_{\max}\right) - d\ln\left(P_{\text{tot}}\right) \tag{3}$$

which can be approximated as:

$$\frac{d\mathrm{EPF}}{\mathrm{EPF}} = \frac{dP_{\max}}{P_{\max}} - \frac{dP_{\mathrm{tot}}}{P_{\mathrm{tot}}} \tag{4}$$

Discretizing this expression over time leads to a linear decomposition of relative trends:

$$\frac{\Delta\,\mathrm{EPF}}{\mathrm{EPF}} \approx \frac{\Delta\,P_{\max}}{P_{\max}} - \frac{\Delta\,P_{\mathrm{tot}}}{P_{\mathrm{tot}}} \tag{5}$$

where $\Delta\,P_{\max}$, $\Delta\,P_{\mathrm{tot}}$, $\Delta\,\mathrm{EPF}$ represent the Sen's slope estimates of the respective variables over the analysis period. Here, the differential form is used as a first-order logarithmic approximation to finite changes over time. In practice, trends are estimated using Sen's slope, and the decomposition represents an approximate linear partitioning of relative changes rather than an exact derivative.

The relative contribution of each component to the overall EPF trend is then computed as:

$$CR_{\max} \approx \frac{\Delta\,P_{\max}/P_{\max}}{\Delta\,\mathrm{EPF}/\mathrm{EPF}} \times 100 \tag{6}$$

$$CR_{\mathrm{tot}} \approx -\frac{\Delta\,P_{\mathrm{tot}}/P_{\mathrm{tot}}}{\Delta\,\mathrm{EPF}/\mathrm{EPF}} \times 100 \tag{7}$$

By construction, the sum of the contributions equals 100%. The sign of each contribution indicates whether that component contributes in the same or opposite direction as the observed EPF trend.

Interpretation of EPF trends requires explicit consideration of relative (percentage) changes in its components. Because EPF is defined as the ratio of annual maximum daily precipitation to total annual precipitation, an increase in EPF does not imply that extremes necessarily intensify or that total precipitation necessarily declines. Rather, EPF increases whenever the fractional rate of change in the annual maximum exceeds that of the annual total. This includes cases in which both quantities increase (or decrease), provided their relative rates differ. Accordingly, EPF trends are interpreted here in terms of proportional changes, not absolute increases or decreases, and are analyzed jointly with a formal decomposition into their component contributions.

Data availability

We used the bias-corrected NASA NEX-GDDP-CMIP6 dataset 86 , which provides daily downscaled climate projections from 25 global climate models participating in CMIP6. The dataset is publicly available through the NASA Center for Climate Simulation (NCCS) at (https://www.nccs.nasa.gov/services/data-collections/land-based-products/nex-gddp-cmip6).

Received: 3 October 2025; Accepted: 2 April 2026
Published online: 21 April 2026

References

1. Gimeno, L. et al. Extreme precipitation events. *WIREs Water*. **9**, e1611 (2022).
2. Kundzewicz, Z. W. Climate change impacts on the hydrological cycle. *Ecohydrol. Hydrobiol.* **8**, 195–203 (2008).
3. Papalexiou, S. M. & Montanari, A. Global and Regional Increase of Precipitation Extremes Under Global Warming. *Water Resour. Res.* **55**, 4901–4914 (2019).
4. Xiong, J. & Yang, Y. Climate Change and Hydrological Extremes. *Curr. Clim. Change Rep.* **11**, 1 (2024).
5. Flannigan, M. D. et al. Fuel moisture sensitivity to temperature and precipitation: climate change implications. *Clim. Change*. **134**, 59–71 (2016).
6. Robinson, W. A. Climate change and extreme weather: A review focusing on the continental United States. *J. Air Waste Manag. Assoc.* **71**, 1186–1209 (2021).
7. Trenberth, K. E. Atmospheric Moisture Residence Times and Cycling: Implications for Rainfall Rates and Climate Change. *Clim. Change*. **39**, 667–694 (1998).
8. Trenberth, K. E. Changes in precipitation with climate change. *Climate Res.* **47**, 123–138 (2011).
9. Dou, T. F., Pan, S. F., Bintanja, R. & Xiao, C. D. More Frequent, Intense, and Extensive Rainfall Events in a Strongly Warming Arctic. *Earth's Future*. **10**, e2021EF002378 (2022).
10. Li, C. et al. Larger Increases in More Extreme Local Precipitation Events as Climate Warms. *Geophys. Res. Lett.* **46**, 6885–6891 (2019).
11. Skeeter, W. J., Senkbeil, J. C. & Keellings, D. J. Spatial and temporal changes in the frequency and magnitude of intense precipitation events in the southeastern United States. *Int. J. Climatol.* **39**, 768–782 (2019).
12. Tian, B. et al. Global scaling of precipitation extremes using near-surface air temperature and dew point temperature. *Environ. Res. Lett.* **18**, 034016 (2023).
13. Alexander, L. V. et al. Global observed changes in daily climate extremes of temperature and precipitation. *J. Geophys. Res. Atmos.* **111**, D05109 (2006).
14. Donat, M. G., Lowry, A. L., Alexander, L. V. & O'Gorman, P. A. Maher, N. More extreme precipitation in the world's dry and wet regions. *Nat. Clim. Change*. **6**, 508–513 (2016).
15. Giorgi, F. & Lionello, P. Climate change projections for the Mediterranean region. *Glob. Planet Change*. **63**, 90–104 (2008).
16. Zhao, J., Gan, T. Y., Zhang, G. & Zhang, S. Projected changes of precipitation extremes in North America using CMIP6 multi-climate model ensembles. *J. Hydrol.* **621**, 129598 (2023).
17. Tabari, H. Climate change impact on flood and extreme precipitation increases with water availability. *Sci. Rep.* **10**, 13768 (2020).
18. Zaerpour, M., Papalexiou, S. M., Pietroniro, A. & Nazemi, A. How extreme are flood peak distributions? A quasi-global analysis of daily discharge records. *J. Hydrol.* **631**, 130849 (2024).
19. Hatami, S. et al. Declining number of northern hemisphere land-surface frozen days under global warming and thinner snowpacks. *Commun. Earth Environ.* https://doi.org/10.1038/s43247-025-03059-6 (2025).
20. Papalexiou, S. M. et al. Sustainability Nexus AID: storms. *SNF* **33**, 1 (2025).

21. Austin, W., Pan, S. & Parthum, B. M. When it Rains, it Pours: Severe Weather Events, Flooding, and Drinking Water Quality. (2024). https://doi.org/10.22004/ag.econ.348901
22. Aggarwal, S., Hu, J. K., Sullivan, J. A., Parks, R. M. & Nethery, R. C. Severe flooding and cause-specific hospitalisation among older adults in the USA: a retrospective matched cohort analysis. *Lancet Planet. Health*. **9**, 101268 (2025).
23. Kron, W. Flood disasters – a global perspective. *Water Policy*. **17**, 6–24 (2015).
24. Pfahl, S., O'Gorman, P. A. & Fischer, E. M. Understanding the regional pattern of projected future changes in extreme precipitation. *Nat. Clim. Change*. **7**, 423–427 (2017).
25. Adler, R. F., Gu, G., Sapiano, M., Wang, J. J. & Huffman, G. J. Global Precipitation: Means, Variations and Trends During the Satellite Era (1979–2014). *Surv. Geophys.* **38**, 679–699 (2017).
26. Asadieh, B. & Krakauer, N. Y. Global trends in extreme precipitation: climate models versus observations. *Hydrol. Earth Syst. Sci.* **19**, 877–891 (2015).
27. Gu, G. & Adler, R. F. Observed variability and trends in global precipitation during 1979–2020. *Clim. Dyn.* **61**, 131–150 (2023).
28. Sun, Q., Zhang, X., Zwiers, F., Westra, S. & Alexander, L. V. A Global, Continental, and Regional Analysis of Changes in Extreme Precipitation. *J. Clim.* **34**, 243–258 (2021).
29. Held, I. M. & Soden, B. J. Robust Responses of the Hydrological Cycle to Global Warming. (2006). https://doi.org/10.1175/JCLI3990.1 doi:10.1175/JCLI3990.1.
30. Oueslati, B., Yiou, P. & Jézéquel, A. Revisiting the dynamic and thermodynamic processes driving the record-breaking January 2014 precipitation in the southern UK. *Sci. Rep.* **9**, 2859 (2019).
31. Saurral, R. I. & Piscitelli, F. M. Dynamic and thermodynamic drivers of rainfall trends at the City of Buenos Aires, Argentina. *Int. J. Climatol.* **43**, 6745–6762 (2023).
32. Nie, J., Sobel, A. H., Shaevitz, D. A. & Wang, S. Dynamic amplification of extreme precipitation sensitivity. *Proceedings of the National Academy of Sciences* 115, 9467–9472 (2018).
33. Fischer, E. M. & Knutti, R. Anthropogenic contribution to global occurrence of heavy-precipitation and high-temperature extremes. *Nat. Clim. Change*. **5**, 560–564 (2015).
34. Box, J. E. et al. Key indicators of Arctic climate change: 1971–2017. *Environ. Res. Lett.* **14**, 045010 (2019).
35. IPCC. : Climate change 2021: The physical science basis. contribution of working group i to the sixth assessment report of the intergovernmental panel on climate change. in *IPCC. (2021). Climate change 2021: The physical science basis. contribution of working group i to the sixth assessment report of the intergovernmental panel on climate change [V. Masson-Delmotte, P. Zhai, A. Pirani, S. L. Connors, C. Péan, S. Berger, N. Caud, et al. (eds.)]. Cambridge University Press.* (2021). https://www.ipcc.ch/report/ar6/wg1/downloads/report/IPCC_AR6_WGI_Citation.pdf (eds Masson-Delmotte, V. et al.) 3–32 (Cambridge University Press, 2021).
36. Giorgi, F., Raffaele, F. & Coppola, E. The response of precipitation characteristics to global warming from climate projections. *Earth Sys. Dyn.* **10**, 73–89 (2019).
37. Trenberth, K. E., Dai, A., Rasmussen, R. M. & Parsons, D. B. The Changing Character of Precipitation. (2003). https://doi.org/10.1175/BAMS-84-9-1205 doi:10.1175/BAMS-84-9-1205.
38. Cortesi, N., Gonzalez-Hidalgo, J. C., Brunetti, M. & Martin-Vide, J. Daily precipitation concentration across Europe 1971–2010. *Nat. Hazards Earth Syst. Sci.* **12**, 2799–2810 (2012).
39. Zaerpour, M. et al. Agriculture's impact on water–energy balance varies across climates. *Proceedings of the National Academy of Sciences* 122, e2410521122 (2025).
40. Zaerpour, M. et al. Impacts of agriculture and snow dynamics on catchment water balance in the U.S. and Great Britain. *Commun. Earth Environ.* **5**, 1–14 (2024).
41. Zittis, G. et al. Climate Change and Weather Extremes in the Eastern Mediterranean and Middle East. *Rev. Geophys.* **60**, e2021RG000762 (2022).
42. Zittis, G., Bruggeman, A. & Lelieveld, J. Revisiting future extreme precipitation trends in the Mediterranean. *Weather Clim. Extremes*. **34**, 100380 (2021).
43. Zaerpour, M. et al. Climate shapes baseflows, influencing drought severity. *Environ. Res. Lett.* **20**, 014035 (2024).
44. Kim, S., Sharma, A., Wasko, C. & Nathan, R. Linking Total Precipitable Water to Precipitation Extremes Globally. *Earth's Future*. **10**, e2021EF002473 (2022).
45. Insua-Costa, D., Lemus-Cánovas, M., Miguez-Macho, G. & Llasat, M. C. Climatology and ranking of hazardous precipitation events in the western Mediterranean area. *Atmos. Res.* **255**, 105521 (2021).
46. Cai, Z. et al. Assessing Arctic wetting: Performances of CMIP6 models and projections of precipitation changes. *Atmos. Res.* **297**, 107124 (2024).
47. Toolan, C. A. et al. Strong intermodel differences and biases in CMIP6 simulations of $PM_{2.5}$, aerosol optical depth, and precipitation over Africa. *Atmos. Chem. Phys.* **25**, 10523–10557 (2025).
48. Prein, A. F. et al. The future intensification of hourly precipitation extremes. *Nat. Clim. Change*. **7**, 48–52 (2017).
49. Pendergrass, A. G. & Hartmann, D. L. Changes in the Distribution of Rain Frequency and Intensity in Response to Global Warming. https://doi.org/10.1175/JCLI-D-14-00183.1 (2014). https://doi.org/10.1175/JCLI-D-14-00183.1
50. Flato, G. et al. Evaluation of climate models. in Climate Change 2013: The Physical Science Basis. Contribution of Working Group I to the Fifth Assessment Report of the Intergovernmental Panel on Climate Change 741–866 (Cambridge University Press, https://doi.org/10.1017/CBO9781107415324.020. (2014).
51. Westra, S. et al. Future changes to the intensity and frequency of short-duration extreme rainfall. *Rev. Geophys.* **52**, 522–555 (2014).
52. Gavasso-Rita, Y. L. et al. Rainfed spring canola yield response to changing heat and water stress in the Canadian Prairie region. *Agric. Water Manage.* **322**, 109966 (2025).
53. Donat, M. G. et al. Global Land-Based Datasets for Monitoring Climatic Extremes. https://journals.ametsoc.org/view/journals/bams/94/7/bams-d-12-00109.1.xml. (2013).
54. Jézéquel, A., Faranda, D., Drobinski, P. & Lionello, P. Extreme Event Attribution in the Mediterranean. *Int. J. Climatol.* **45**, e8799 (2025).
55. Lazoglou, G. et al. Identification of climate change hotspots in the Mediterranean. *Sci. Rep.* **14**, 29817 (2024).
56. Ballarin, A. S. et al. Frequency Rather Than Intensity Drives Projected Changes of Rainfall Events in Brazil. *Earth's Future* 12, eEF004053 (2024). (2023).
57. Ho, M. et al. Changes in flood-associated rainfall losses under climate change. *J. Hydrol.* **625**, 129950 (2023).
58. Ballarin, A. S. et al. Drought intensification in Brazilian catchments: implications for water and land management. *Environ. Res. Lett.* **19**, 054030 (2024).
59. Papalexiou, S. M. et al. Probabilistic Evaluation of Drought in CMIP6 Simulations. *Earth's Future*. **9**, 002150 (2021). e2021EF.
60. Myhre, G. et al. Frequency of extreme precipitation increases extensively with event rareness under global warming. *Sci. Rep.* **9**, 16063 (2019).
61. Pendergrass, A. G. What precipitation is extreme? *Science* **360**, 1072–1073 (2018).
62. Case, J. L. et al. Soil Moisture Responses Associated with Significant Tropical Cyclone Rainfall Events. (2021). https://repository.library.noaa.gov/view/noaa/63683
63. Tooth, S. Process, form and change in dryland rivers: a review of recent research. *Earth Sci. Rev.* **51**, 67–107 (2000).
64. *Hydrological Modelling in Arid and Semi-Arid Areas.* (Cambridge University Press, Cambridge, (2007). https://doi.org/10.1017/CBO9780511535734
65. Walsh, J. E. Intensified warming of the Arctic: Causes and impacts on middle latitudes. *Glob. Planet Change*. **117**, 52–63 (2014).

66. Wang, K. et al. Continuously amplified warming in the Alaskan Arctic: Implications for estimating global warming hiatus. *Geophys. Res. Lett.* **44**, 9029–9038 (2017).
67. Bintanja, R. & Andry, O. Towards a rain-dominated Arctic. *Nat. Clim. Change*. **7**, 263–267 (2017).
68. McCrystall, M. R., Stroeve, J., Serreze, M., Forbes, B. C. & Screen, J. A. New climate models reveal faster and larger increases in Arctic precipitation than previously projected. *Nat. Commun.* **12**, 6765 (2021).
69. Yu, L. & Zhong, S. Trends in Arctic seasonal and extreme precipitation in recent decades. *Theor. Appl. Climatol*. **145**, 1541–1559 (2021).
70. Kattsov, V. M. et al. Simulation and Projection of Arctic Freshwater Budget Components by the IPCC AR4 Global Climate Models. (2007). https://doi.org/10.1175/JHM575.1 doi:10.1175/JHM575.1.
71. Lionello, P. et al. The climate of the Mediterranean region: research progress and climate change impacts. *Reg. Environ. Change*. **14**, 1679–1684 (2014).
72. Lionello, P. & Scarascia, L. The relation between climate change in the Mediterranean region and global warming. *Reg. Environ. Change*. **18**, 1481–1493 (2018).
73. Noto, L. V., Cipolla, G., Pumo, D. & Francipane, A. Climate Change in the Mediterranean Basin (Part II): A Review of Challenges and Uncertainties in Climate Change Modeling and Impact Analyses. *Water Resour. Manage.* **37**, 2307–2323 (2023).
74. Philandras, C. M. et al. Long term precipitation trends and variability within the Mediterranean region. *Nat. Hazards Earth Syst. Sci.* **11**, 3235–3250 (2011).
75. Tramblay, Y. & Somot, S. Future evolution of extreme precipitation in the Mediterranean. *Clim. Change*. **151**, 289–302 (2018).
76. Christensen, J. H. et al. Regional climate projections. In: *Climate Change 2007: The Physical Science Basis. Contribution of Working Group I to the Fourth Assessment Report of the Intergovernmental Panel on Climate Change* (eds Solomon, S. et al.) (Cambridge University Press, Cambridge, New York, 2007).
77. Cos, J. et al. The Mediterranean climate change hotspot in the CMIP5 and CMIP6 projections. *Earth Sys. Dyn.* **13**, 321–340 (2022).
78. Ulbrich, U. et al. Past and Current Climate Changes in the Mediterranean Region. in Regional Assessment of Climate Change in the Mediterranean: Volume 1: Air, Sea and Precipitation and Water (eds (eds Navarra, A. & Tubiana, L.) 9–51 (Springer Netherlands, Dordrecht, doi:https://doi.org/10.1007/978-94-007-5781-3_2. (2013).
79. Miró, J. J., Estrela, M. J., Corell, D., Gómez, I. & Luna, M. Y. Precipitation and drought trends (1952–2021) in a key hydrological recharge area of the eastern Iberian Peninsula. *Atmos. Res.* **286**, 106695 (2023).
80. Gründemann, G. J., van de Giesen, N., Brunner, L. & van der Ent, R. Rarest rainfall events will see the greatest relative increase in magnitude under future climate change. *Commun. Earth Environ.* **3**, 235 (2022).
81. Jong, B. T., Delworth, T. L., Cooke, W. F., Tseng, K. C. & Murakami, H. Increases in extreme precipitation over the Northeast United States using high-resolution climate model simulations. *npj Clim. Atmos. Sci.* **6**, 18 (2023).
82. Thackeray, C. W., Hall, A., Norris, J. & Chen, D. Constraining the increased frequency of global precipitation extremes under warming. *Nat. Clim. Chang.* **12**, 441–448 (2022).
83. Zhang, B., Song, S., Wang, H., Guo, T. & Ding, Y. Evaluation of the performance of CMIP6 models in simulating extreme precipitation and its projected changes in global climate regions. *Nat. Hazards*. **121**, 1737–1763 (2025).
84. Bintanja, R. & Selten, F. M. Future increases in Arctic precipitation linked to local evaporation and sea-ice retreat. *Nature* **509**, 479–482 (2014).
85. Thrasher, B. et al. NASA Global Daily Downscaled Projections, CMIP6. *Sci. Data*. **9**, 262 (2022).
86. Eyring, V. et al. Overview of the Coupled Model Intercomparison Project Phase 6 (CMIP6) experimental design and organization. *Geosci. Model Dev.* **9**, 1937–1958 (2016).
87. Maraun, D. et al. Precipitation downscaling under climate change: Recent developments to bridge the gap between dynamical models and the end user. *Rev. Geophys.* **48**, RG3003 (2010).
88. Bao, Y. & Wen, X. Projection of China's near- and long-term climate in a new high-resolution daily downscaled dataset NEX-GDDP. *J. Meteorol. Res.* **31**, 236–249 (2017).
89. Cao, F. et al. Projected Effects of Climate Change on Meteorological Droughts over China: A Study Based on High-Resolution NEX-GDDP Data. https://doi.org/10.1175/JHM-D-23-0178.1 (2025). https://doi.org/10.1175/JHM-D-23-0178.1
90. Das, S., Das, J. & Umamahesh, N. V. Identification of future meteorological drought hotspots over Indian region: A study based on NEX-GDDP data. *Int. J. Climatol.* **41**, 5644–5662 (2021).
91. Jain, S., Salunke, P., Mishra, S. K., Sahany, S. & Choudhary, N. Advantage of NEX-GDDP over CMIP5 and CORDEX Data: Indian Summer Monsoon. *Atmos. Res.* **228**, 152–160 (2019).
92. Koohi, S. & Ramezani Etedali, H. Future meteorological drought conditions in southwestern Iran based on the NEX-GDDP climate dataset. *J. Arid Land.* **15**, 377–392 (2023).
93. Beck, H. E. et al. Present and future Köppen-Geiger climate classification maps at 1-km resolution. *Sci. Data*. **5**, 180214 (2018).
94. Princeton Global Forcings Global Meteorological Forcing Dataset for Land Surface Modeling. *NSF Natl. Cent. Atmospheric Res.* https://doi.org/10.5065/JV89-AH11 (2018).
95. Sheffield, J., Goteti, G. & Wood, E. F. Development of a 50-Year High-Resolution Global Dataset of Meteorological Forcings for Land Surface Modeling. (2006). https://doi.org/10.1175/JCLI3790.1 doi:10.1175/JCLI3790.1.
96. Kendall, M. G. *Rank Correlation Methods*. (Griffin, Oxford, England, (1948).
97. Mann, H. B. Nonparametric Tests Against Trend. *Econometrica* **13**, 245–259 (1945).
98. Hirsch, R. M. & Slack, J. R. A Nonparametric Trend Test for Seasonal Data With Serial Dependence. *Water Resour. Res.* **20**, 727–732 (1984).
99. Sen, P. K. Estimates of the Regression Coefficient Based on Kendall's Tau. *J. Am. Stat. Assoc.* **63**, 1379–1389 (1968).

Author contributions

M.Z. led the conceptualization, methodology, investigation, visualization, and writing—original draft. S.M.P. contributed to the conceptualization, methodology, and writing—original draft. G.T. contributed to the investigation and writing—original draft. All authors participated in review and editing of the manuscript.

Funding

This study was supported by the Natural Sciences and Engineering Research Council of Canada (NSERC Discovery Grant: RGPIN-2019-06894).

Declarations

Competing interests

The authors declare no competing interests.

Additional information

Supplementary Information The online version contains supplementary material available at https://doi.org/10.1038/s41598-026-47708-y.

Correspondence and requests for materials should be addressed to M.Z. or G.T.